

Application of the Diamond Gate in Quantum Fourier Transformations and Quantum Machine Learning

E. Bahnsen,¹ S. E. Rasmussen,¹ N. J. S. Loft,¹ and N. T. Zinner^{1,2,*}

¹*Department of Physics and Astronomy, Aarhus University, DK-8000 Aarhus C, Denmark*

²*Aarhus Institute of Advanced Studies, Aarhus University, DK-8000 Aarhus C, Denmark*

(Dated: March 10, 2022)

As we are approaching actual application of quantum technology, it is essential to exploit the current quantum resources in the best possible way. With this in mind, it might not be beneficial to use the usual standard gate sets, inspired from classical logic gates, when compiling quantum algorithms when other less standardized gates currently perform better. We, therefore, consider a promising native gate, which occurs naturally in superconducting circuits, known as the diamond gate. We show how the diamond gate can be decomposed into standard gates and, using single-qubit gates, can work as a controlled-not-swap (CNS) gate. We then show how this CNS gate can create a controlled phase gate. Controlled phase gates are the backbone of the quantum Fourier transform algorithm, and we, therefore, show how to use the diamond gate to perform this algorithm. We also show how to use the diamond gate in quantum machine learning; namely, we use it to approximate non-linear functions and classify two-dimensional data.

I. INTRODUCTION

Quantum technology has gained an increasing amount of attention in the past couple of years, especially since the quantum supremacy experiment at Google [1]. The search for quantum advantages in practical applications is an increasingly active area of research [2], and there is a growing consensus that practical applications will be found in the noisy intermediate-scale quantum (NISQ) era [3]. In this era, quantum technology supports only a couple of tens of qubits and a few hundred gate operations before the noise becomes too overwhelming.

In this era, we must work with the native gates of quantum systems, despite their imperfections compared to the set of standard gates, composed of gates such as the CNOT or Fredkin gate. An example of such a native gate is the diamond gate [4], which has the advantage of being a naturally arising highly entangling four-qubit gate in superconducting circuits. However, it has the disadvantage of being a complex gate to understand and thus use in quantum algorithm circuits. This paper seeks to interpret the gate and show its various applications in synthesizing other quantum gates, performing quantum algorithms, and participating in quantum machine learning. This paper aims to show the utility of the diamond gate and show a different approach to quantum circuitry using some currently available gates rather than some of the standard gates.

The diamond gate is closely related to the Fredkin gate, which is often used in a set of standard gates for quantum computation [5]. In particular, they are both controlled-swapping gates; however, the diamond has a pair of control qubits, which must be in a Bell state for the closed state of the gate. Other implementations of controlled-swapping gates besides the Fredkin gate [6–14]

include superconducting qubits in a waveguide cavity [15], linear superconducting qubits [16], and multicontrolled i SWAP gates [17].

A popular approach to optimize the computational power is to divide the computational task between classical and quantum resources, i.e., a so-called hybrid quantum classical (HQC) algorithm. Examples of such HQC algorithms are the quantum approximate optimization algorithm (QAOA) [18–20], the quantum autoencoder (QAE) [21], the quantum variational error corrector (QVECTOR) [22], classification via the near term-quantum neural network (QNN) [23–26], the quantum generative adversarial network (QuGAN) [27–30], and the variational quantum eigensolver (VQE) [31–38].

Common to all these HQC algorithms is that they share a subroutine for producing parameterized trial states, where the parameters can be tuned to optimize a function value. The performance of these algorithms depends on the configuration of the parameterized quantum circuit (PQC) [39–42]. Many of the HQC algorithms draw inspiration from classical machine-learning algorithms. Therefore, PQCs are often considered the quantum-mechanical equivalent of neural networks, which is why they are sometimes referred to as quantum neural networks [23–26]. In this paper, we apply the diamond gate to quantum circuit learning [43] and classification via QNNs [26], using the diamond gate as an entangling gate in a PQC. Previously, it has been shown that the diamond gate could be useful in VQE algorithms [44]. Besides HQC algorithms, we also consider the diamond gate for performing quantum Fourier transformations (QFT), which are used to estimate the phase of quantum-mechanical amplitudes. This could be used to solve the order-finding problem or the factoring problem [5].

The rest of the paper is structured as follows. In Section II, we introduce the diamond gate and its main properties. In Section III, we show how to change the diamond gate into a combined SWAP and CNOT gate, also known as the CNS gate. Then, in Section IV, we sym-

* zinner@phys.au.dk

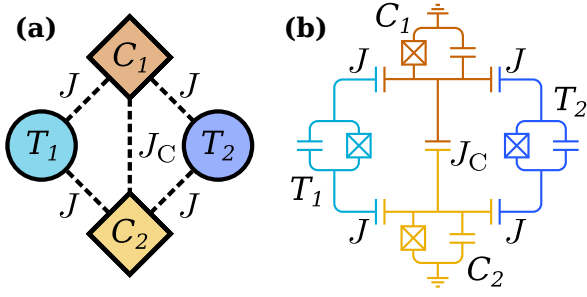


Figure 1. **(a)** A four-qubit system of two control qubits (C_1 and C_2) and two target qubits (T_1 and T_2), which constitutes the diamond circuit. These couple through their exchange interaction with strengths J and J_C as indicated. **(b)** An equivalent simple circuit diagram of superconducting transmon qubits, which are capacitively coupled with the same strengths J and J_C . Figure reproduced, with permission, from Ref. [4].

metrically decompose the diamond gate into standard gates while preserving its symmetry. Using this decomposition, we show in Section V that the diamond gate can be operated as a native controlled-phase gate. We then, in Section VI, use this to perform the quantum Fourier transform with the diamond gate. In Section VII we apply the diamond gate to machine-learning problems. In particular, we apply it to a problem of quantum circuit learning [43] and classification of two-dimensional data [26]. Finally, in Section VIII, we present our conclusion and the outlook.

II. THE FOUR-QUBIT DIAMOND GATE

The algorithms presented in this paper are based upon the diamond gate developed in Ref. [4]; therefore, we only offer an overview and details can be found in the original paper.

The diamond gate is a highly entangled four-qubit gate natively implemented using superconducting circuits. The system consists of two target qubits (T_1 and T_2) and two control qubits (C_1 and C_2). Each pair of control and target qubits is connected with a coupling strength of J . The two control qubits are coupled with a coupling strength of J_C . The system schematics can be seen in Fig. 1(a). A superconducting circuit design resulting in the diamond gate could consist of transmonlike qubits [45, 46] coupled by capacitors, as seen in Fig. 1(b).

Using units where $\hbar = 1$, the system is governed by the Hamiltonian

$$H = -\frac{1}{2}(\Omega + \Delta)(\sigma_z^{T_1} + \sigma_z^{T_2}) - \frac{1}{2}\Omega(\sigma_z^{C_1} + \sigma_z^{C_2}) + J_C\sigma_y^{C_1}\sigma_y^{C_2} + J(\sigma_y^{T_1} + \sigma_y^{T_2})(\sigma_y^{C_1} + \sigma_y^{C_2}), \quad (1)$$

where $\sigma_{x,y,z}^j$ are the Pauli operators acting on the j th qubit. The target qubits are in resonance with each other, with frequency $\Omega + \Delta$, while the control qubits are in resonance with frequency Ω .

Assuming that $|2\Omega| \gg |J|$ and $|\Delta| \gg |J|, |J_C|$ the time-evolution operator of the diamond circuit takes the form

$$U(t) = |00\rangle\langle 00| \otimes U_T^{00}(t) + |11\rangle\langle 11| \otimes U_T^{11}(t) + |\Psi^+\rangle\langle \Psi^+| \otimes U_T^{\Psi^+}(t) + |\Psi^-\rangle\langle \Psi^-| \otimes U_T^{\Psi^-}(t), \quad (2)$$

where the unitary U_T^i act on the target qubits, while the operators, $|C_1C_2\rangle\langle C_1C_2|$, acts on the control qubits, with C_1 and C_2 representing the first and second control qubit, respectively. These can be in either of the control states $|00\rangle, |11\rangle, |\Psi^+\rangle, |\Psi^-\rangle$, where $|\Psi^\pm\rangle = (|01\rangle \pm |10\rangle)/\sqrt{2}$ are the Bell states. From Eq. (2), we realize that $U(t)$ is block diagonal in this basis, which we call the Bell basis. The unitaries of the target qubits are (represented in the computational basis $|T_1T_2\rangle \in \{|00\rangle, |01\rangle, |10\rangle, |11\rangle\}$, which is used unless noted otherwise)

$$U_T^{00}(t) = \begin{pmatrix} 1 & 0 & 0 & 0 \\ 0 & \frac{1}{2}(e^{-i\zeta t} + 1) & \frac{1}{2}(e^{-i\zeta t} - 1) & 0 \\ 0 & \frac{1}{2}(e^{-i\zeta t} - 1) & \frac{1}{2}(e^{-i\zeta t} + 1) & 0 \\ 0 & 0 & 0 & e^{-i\zeta t} \end{pmatrix}, \quad (3a)$$

$$U_T^{11}(t) = \begin{pmatrix} e^{i\zeta t} & 0 & 0 & 0 \\ 0 & \frac{1}{2}(e^{i\zeta t} + 1) & \frac{1}{2}(e^{i\zeta t} - 1) & 0 \\ 0 & \frac{1}{2}(e^{i\zeta t} - 1) & \frac{1}{2}(e^{i\zeta t} + 1) & 0 \\ 0 & 0 & 0 & 1 \end{pmatrix}, \quad (3b)$$

$$U_T^{\Psi^+}(t) = \begin{pmatrix} e^{i\zeta t} & 0 & 0 & 0 \\ 0 & 1 & 0 & 0 \\ 0 & 0 & 1 & 0 \\ 0 & 0 & 0 & e^{-i\zeta t} \end{pmatrix} e^{-iJ_C t}, \quad (3c)$$

$$U_T^{\Psi^-}(t) = \begin{pmatrix} 1 & 0 & 0 & 0 \\ 0 & 1 & 0 & 0 \\ 0 & 0 & 1 & 0 \\ 0 & 0 & 0 & 1 \end{pmatrix} e^{+iJ_C t}, \quad (3d)$$

where $\zeta = 4J^2/\Delta$. If we consider a gate time of $t_g = \pi/\zeta$, the unitaries of the target qubits can be written in standard gates as

$$U_T^{00}(t_g) = ZZ \times CZ \times \text{SWAP}, \quad (4a)$$

$$U_T^{11}(t_g) = -CZ \times \text{SWAP}, \quad (4b)$$

$$U_T^{\Psi^+}(t_g) = -ZZ \times e^{-iJ_C t_g}, \quad (4c)$$

$$U_T^{\Psi^-}(t_g) = \Pi \times e^{+iJ_C t_g}, \quad (4d)$$

where we use the notation that $ZZ = Z \otimes Z$ is a Z gate on each of the target qubits. Without external interactions and depending on the choice of coupling strengths, J and J_C , the diamond gate can operate with fidelities above 0.99 and a gate time around 60 ns. Since it only contributes a phase, we set $J_C = 0$ for simplicity.

III. CNS EQUIVALENT CIRCUIT

This section shows that the diamond gate, together with single-qubit rotations, can produce the useful CNS

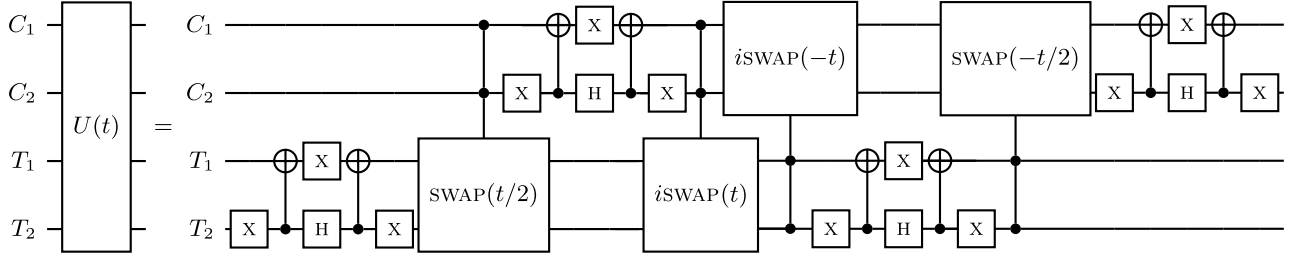


Figure 2. Standard gate decompositions of the diamond gate with no control coupling, $J_C = 0$, and application time t . The circuit employs two double-controlled parameterized i SWAP gates and two double-controlled parameterized SWAP gates.

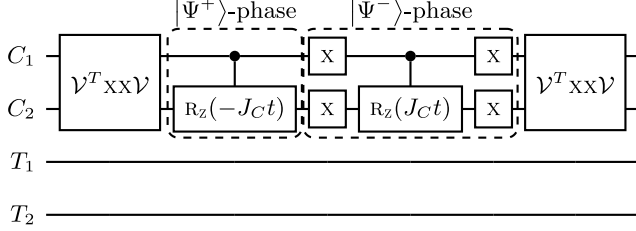


Figure 3. The Circuit diagram of how to add the functionality of the global phases that the diamond gate applies if $J_C \neq 0$. If the control qubits are in the state $|\Psi^\pm\rangle$, the phase $e^{\mp i J_C t}$ is applied. To add this functionality, we have to concatenate this to the end of the diagram of the diamond gate.

implementation of the controlled R_n gate (see Fig. 5)

$$R_n = R_z(2\pi/2^n) = \begin{pmatrix} 1 & 0 \\ 0 & e^{2\pi i/2^n} \end{pmatrix}. \quad (9)$$

Such a gate can be implemented following the prescription in Ref. [65], in which different ways of decomposing the controlled R_n gate are derived, but we use the approach with one auxiliary qubit, such that three of the four diamond qubits are in use like so:

$$|0\rangle \text{---} \text{---} |0\rangle \quad |0\rangle \text{---} \text{---} |0\rangle \quad (10)$$

which locks one of the qubits in the $|0\rangle$ state. Our approach uses diamond instead of controlled-SWAP gates. This introduces one extra qubit and, due to the symmetry of the diamond gate, we can pick this to be any of the four diamond qubits. We choose C_2 for this task and fix it in a $|1\rangle$ state. We then pick the other control qubit, C_1 , as the control of the above R_n gate, while we choose T_1 as the target and, finally, T_2 will be the ancillary qubit in the $|0\rangle$ state. The circuit diagram takes the form

$$|C_1\rangle \text{---} |1\rangle \text{---} |T_1\rangle \text{---} |0\rangle \quad = \quad |C_1\rangle \text{---} |1\rangle \text{---} |T_1\rangle \text{---} |0\rangle \quad (11)$$

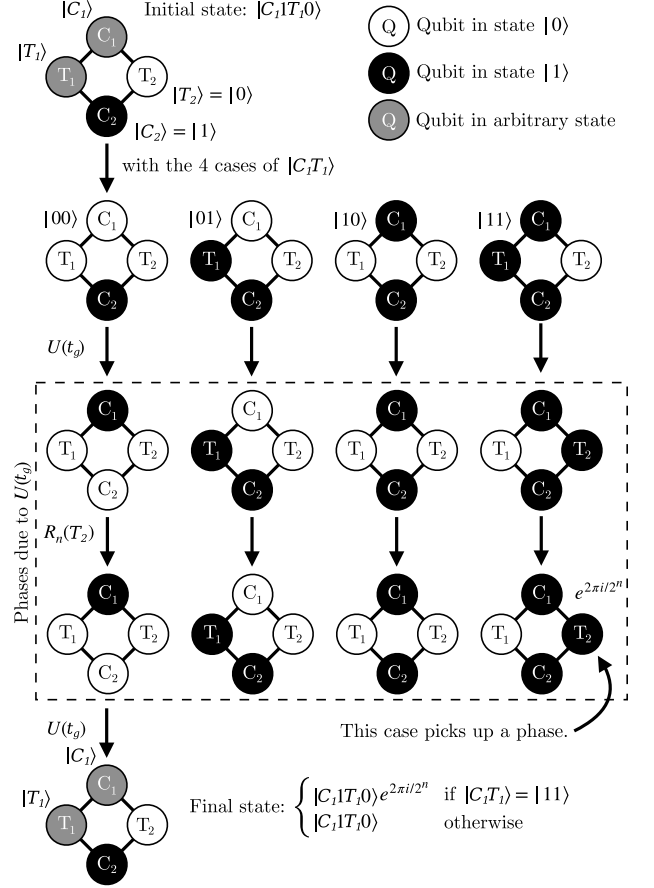


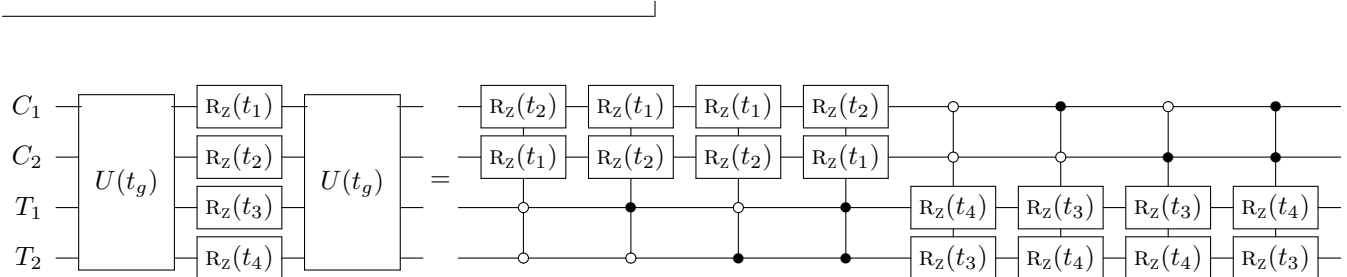
Figure 4. The flow chart of how the native diamond gate may implement a controlled R_n gate. The qubits start in the state $|C_1 T_1 0\rangle$ and will by the end pick up a phase $e^{2\pi i/2^n}$ if and only if both the control and the target qubit are in the $|1\rangle$ state. The flow chart corresponds to the circuit diagram in Eq. (11).

Note that per Eq. (4), the diamond gate introduces both a SWAP and a CZ gate, contrary to Eq. (10), where we only need a SWAP gate. However, the second diamond gate cancels out the CZ gate of the first diamond gate, making Eq. (11) equivalent to Eq. (10).

In order to understand the circuit diagram in Eq. (11), we consider the four different possibilities for two undetermined qubits C_1 and T_1 , i.e., we consider the four

different possibilities for the state $|C_1T_1\rangle$. Note that the four possibilities we consider are a complete basis for the two qubits. We want the qubit to obtain an overall factor $e^{2\pi i/2^n}$ only when $|C_1T_1\rangle = |11\rangle$. The four different cases are presented in Fig. 4, from which we see that the phase is only obtained in the desired case.

We start with the one control and one target qubit in the state $|C_2T_2\rangle = |10\rangle$, while the two other qubits are in an arbitrary state $|C_1T_1\rangle$. In Fig. 4, we branch out to the four different possibilities $|0100\rangle$, $|0110\rangle$, $|1100\rangle$, and $|1110\rangle$. When we apply the first $U(t_g)$ gate, we effectively compare the states of control qubits C_1 and C_2 and if they are equal, the states of T_1 and T_2 are swapped. This happens in the fourth branch of Fig. 4. In the third branch, the states of the target qubits are the same, as is also the case for the control qubit. The states of the two target qubits do swap, and the same is the case for the two control qubits; however, as the states are the same for each pair of qubits, we do not observe this swapping. Due



This allows us to program what controlled-phase gates to keep, by fixing the states of some of the qubits, as well as choosing different values of t_i . If we set $t_1 = t_2 = t_3 = 0$ and $t_4 = 2\pi/2^n$ and initiate qubits C_2 and T_2 to $|C_2T_2\rangle = |10\rangle$, we obtain the result in Eq. (11) from above. Note that the open circles in the above circuit represent control qubits conditional on the control qubit being in the state $|0\rangle$. These are related to the solid circles, which are control qubits conditional on the qubit being in the state $|1\rangle$, by performing a X gate before and after the control qubit [5].

VI. NATIVE QFT ALGORITHM WITH THE DIAMOND GATE

Having found a way to apply a controlled R_n gate to all qubits using the diamond gate, we are now ready to consider the problem of performing the quantum Fourier-transformation algorithm. This can be done using the circuit seen in Fig. 5. If $|j\rangle$ is a ket in an orthonormal basis, $\{|0\rangle, |1\rangle, \dots, |N-1\rangle\}$, this circuit performs the transformation

$$|j\rangle \mapsto \frac{1}{\sqrt{N}} \sum_{k=0}^{N-1} e^{2\pi ijk/2^n} |k\rangle, \quad (12)$$

to the symmetry of the diamond gate, the target qubits' states are also compared and the states of the control qubits are swapped accordingly. This is what happens in the first branch. The target qubit states are different in the second branch, and no control state is swapped. When we apply the $R_n^{T_2}$ gate, only the fourth branch picks up the phase, as it is the only case for which T_2 is in the $|1\rangle$ state. Finally, when we apply the $U(t_g)$ gate again, we swap the states back and the qubits obtain an overall phase if and only if the original state is $|1110\rangle$.

A. Phase programming

Since the diamond gate is symmetric in the target and control qubits, we can place phase gates on all qubits between the two diamond gates and obtain controlled-phase gates on all qubits. Doing this, we obtain the following circuit:

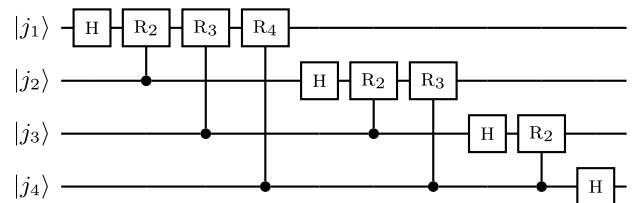


Figure 5. Quantum Fourier-transform circuit with four qubits [5].

where $N = 2^n$, in which n is the number of qubits, and $|k\rangle$ denotes the k th basis state [5].

We must first arrange the qubits as we wish in order to perform the QFT algorithm using the diamond gate. As a starting point, we choose to arrange the qubits in two parallel lines as shown in Fig. 6. The upper line contains the target qubits in arbitrary states $|j_1\rangle, \dots, |j_n\rangle$, while the lower line shows the auxiliary qubits, all in states $|0\rangle$. Tuning a square of these qubits into resonance makes it possible to perform the diamond gate. This arrangement of qubits is a simple implementation of QFT; however, for many qubits, frequency crowding might lead to an unwanted crosstalk between qubits. In Appendix A, we present alternative arrangements of qubits, which make this problem less severe.

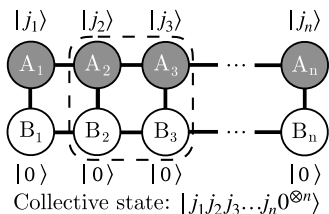


Figure 6. Two parallel interconnected lines of qubits are used in the QFT algorithm. The upper qubits (A) are initialized in the states $|j_1\rangle, \dots, |j_n\rangle$, while the lower qubits (B) are all in the $|0\rangle$ state. A diamond gate can be performed using one pair of A qubits and one pair of B qubits.

A. QFT algorithm

Here, we present an algorithm for QFT using the topology presented in Fig. 6:

Algorithm 1 Native-Gate-Assisted QFT on Double String of Qubits

- 1: Initialize qubits A_1, \dots, A_n with the states to transform
 - 2: Initialize qubits B_1, \dots, B_n in state $|0\rangle^{\otimes n}$
 - 3: **for** $i = 1$ **to** n **do** ▷ For every target state
 - 4: H on A_i
 - 5: **for** $j = i + 1$ **to** n **do** ▷ ...for every control state
 - 6: X on B_{j-1} ▷ Do CR_n using native gate
 - 7: $U(t_g)$ on $(A_j, B_{j-1}, A_{j-1}, B_j)$
 - 8: R_{j-i+1} on B_j
 - 9: $U(t_g)$ on $(A_j, B_{j-1}, A_{j-1}, B_j)$
 - 10: X on B_{j-1}
 - 11: **if** $j \neq n$ **then** ▷ Swap along chain (except last)
 - 12: $iSWAP(t_g/2)$ on (A_{j-1}, A_j)
 - 13: **end if**
 - 14: **end for**
 - 15: **for** $j = n - 1$ **to** $i + 1$ **do** ▷ Swap state back home
 - 16: $iSWAP(3t_g/2)$ on (A_{j-1}, A_j)
 - 17: **end for** ▷ Done for A_i
 - 18: **end for**
 - 19: Reverse order of A qubits.
-

The algorithm iterates through every A qubit, from A_1 (of state $|j_1\rangle$) to A_n (of state $|j_n\rangle$). First, a Hadamard gate is applied to the A_i th qubit. Then a phase gate is applied to the same qubit, controlled by its neighboring A qubit (A_{i+1}), based upon the diamond-gate-assisted controlled R_n gate of Eq. (11). This diamond gate is formed by tuning the diamond of A qubits (A_i and A_{i+1}) and the associated pair of B qubits (B_i and B_{i+1}). Then, the pair of A qubits swaps states through an $iSWAP$ gate, such that another controlled phase may be applied to the A_{i+1} th qubit, which now holds the state of the A_i th qubit. This is repeated such that the original state of the A_i th qubit is swapped to the end of the chain. At this point, it is swapped back into place by doing the $iSWAP$ s in reverse.

Note that the initial swaps down the chain are $iSWAP(t_g/2)$, whereas the ones on the way back are $iSWAP(3t_g/2)$. Simply doing $iSWAP(t_g/2)$ twice could leave

the pair of states with unwanted phases but using $iSWAP(3t_g/2)$ the second time around gets rid of these. Indeed, the trick here is that by swapping the states back through the chain, we ensure that each swapped pair of states will see each other twice. In turn, this will cancel any phase introduced by the initial $iSWAP(t_g/2)$. An example of this algorithm for $n = 4$ can be found in Appendix B.

This QFT implementation on $O(n)$ input states requires $2n$ qubits. Thus, the number of qubits required grows linearly with the input size. The circuit depth grows as $O(n^2)$ as the standard QFT algorithm. On top of that, we can adapt the method of the approximate QFT and leave out the smallest of the R_n angles. This reduces the depth to grow as $O(n \log n)$. Nevertheless, in absolute gate numbers, it does use more than regular QFT because we have to swap the states along the chain. The absolute gate counts are thus

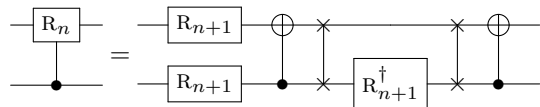
- n H gates
- $n(n + 1)$ X gates
- $n(n + 1)/2$ R_n gates
- $n(n - 1)$ $iSWAP$ gates

This is without considering the QFT cross-swap of the A qubits at the end. Still, the algorithmic part of this procedure does not add asymptotic overhead to the existing QFT algorithm. In other words, the QFT algorithm with the diamond algorithm has neither an advantage nor a disadvantage over the QFT algorithm with standard gates; it is merely an alternative formulation of the algorithm.

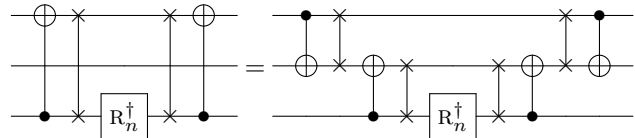
B. Native-CNS-gate-based QFT algorithm

We wish to implement the QFT algorithm using the diamond version of the CNS gate in Section III.

Using an identity from Ref. [65], we replace each controlled R_n gate and introduce a pair of swaps to create two CNS gates:



Now, the diamond circuit can only execute CNS gates on opposing qubits, and for the QFT algorithm in Fig. 5, we have to operate between all qubits. However, the CNS gate can also be used to make a pseudoswap gate for this purpose. Thus, we use pairs of CNS gates to swap the first qubit into place and back again as follows:



This works because of the symmetry of the swapping CNS gate pairs: the qubit at the control will only pick

up a phase between each pair, and the target one is not transformed at all. Therefore, the effects of the CNS gates will cancel each other; however, we can still utilize the swapping functionality in between.

This algorithm can be run on a chain of diamond circuits, having the CNS gates only work on adjacent qubits. However, this sequence of gates can still be significantly refactored using the identity

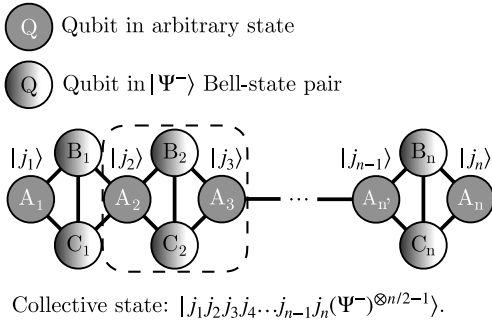
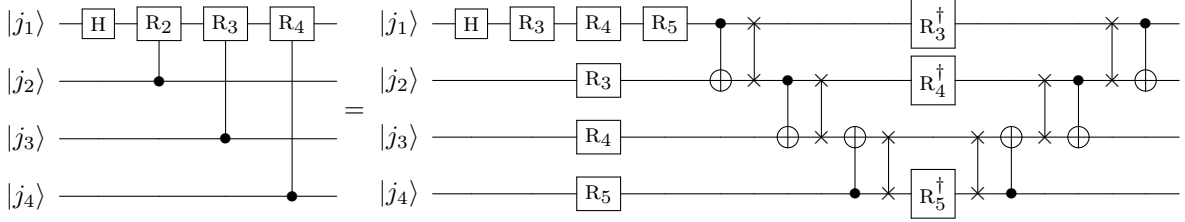
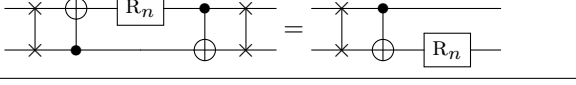


Figure 7. A chain of concatenated diamond circuits, each sharing a target qubit with its neighbor. This arrangement can be used to execute a CNS gate-assisted QFT algorithm.

Now, three similar circuits have to be added to represent the QFT of all four qubits. In the same way, this method can be extended to more qubits. In particular, one hardware setup to execute this algorithm is seen in Fig. 7, which is just a sequence of concatenated diamond circuits, each sharing one qubit with its neighbor. Using this configuration, an additional QFT qubit requires three extra qubits in the circuit, i.e., QFT on n qubits requires $3n + 1$ circuit qubits.

VII. QUANTUM MACHINE LEARNING WITH THE DIAMOND GATE

Another application where the diamond gate could prove helpful is in hybrid quantum-classical algorithms. Examples of this have already been shown with variational quantum eigensolvers [44]. Here, we wish to consider the

Finally, this means that we can write the first part of the QFT algorithm in Fig. 5, which is the QFT of the first qubit, as

diamond gate in an HQC algorithm for machine learning on near-term quantum processors, namely quantum circuit learning as proposed by Ref. [43]. Besides quantum circuit learning, we also wish to consider the problem of classifying data using PQCs with the diamond gate as an entangling gate. We do this following the approach taken by Ref. [26].

A. Quantum circuit learning

Quantum circuit learning is quantum-aided machine learning and can approximate nonlinear functions. In Ref. [43], it is argued that quantum circuit learning might have an advantage over classical approximators when it comes to more complex functions. This is because the computational cost of classical learning increases with the number of basis functions needed to represent complex functions. Quantum circuit learning, on the other hand, directly utilizes the exponential number of functions concerning the number of qubits to model the teacher. However, the approximation of such complex functions is beyond the capabilities of the current state-of-the-art quantum technology and we, therefore, approximate more straightforward functions. Quantum circuit learning is done in five steps:

1. Encode input data in some quantum state $|\psi_{\text{in}}(x)\rangle = U_1(x)|0\dots 0\rangle$.
2. Apply parameterized quantum circuit to the input state $|\psi_{\text{out}}(\theta_i, x)\rangle = U_2(\theta_i)|\psi_{\text{in}}(x)\rangle$.
3. Measure expectation values of some set of observables, $\{B_k\}$, by using some output function F , the output is defined to be $y(x, \theta_i) = F(\{B_k(x, \theta_i)\})$.

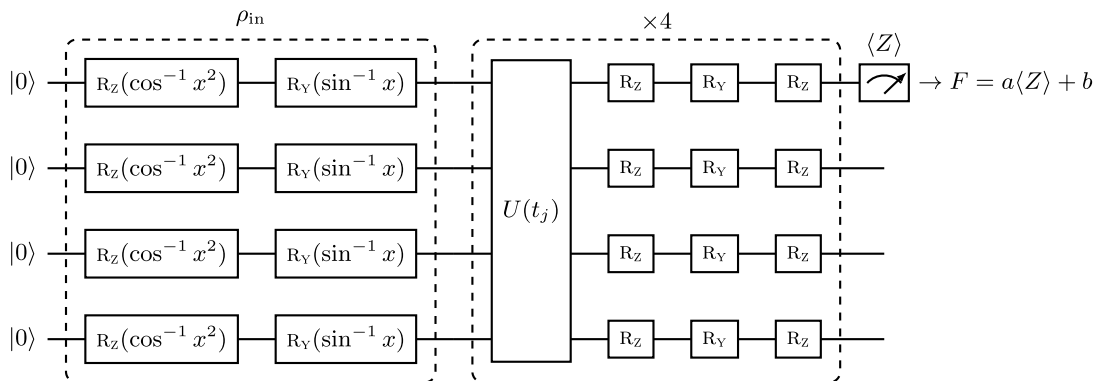


Figure 8. The circuit diagram of diamond-gate-aided circuit learning. The input data are encoded into the density matrix ρ_{in} using R_z and R_y rotations on each qubit, which yield a state similar to Eq. (13). This happens in the left dashed box. The diamond gate, $U(t)$, acts as an entangling gate between the single-qubit rotations. The diamond-gate and single-qubit rotations in the right dashed box are repeated four times, with different rotations each time, yielding a four-layered parameterized quantum circuit. In the end, the first qubit is measured in the Z basis and the output is scaled and shifted. We optimize the parameters a , b , and t_j , as well as the rotation angles of the single-qubit rotations in the right box.

4. Minimize the cost function $L(f(x), y(x, \theta_i))$ of the objective function $f(x)$ and output by tuning the parameters θ_i .
5. Evaluate the performance by checking the value of the cost function or a similar evaluation criterion.

We wish to use the diamond gate for approximating a function of one parameter $f: [-1, 1] \rightarrow \mathbb{R}$. We, therefore, encode a quantum state as the density matrix

$$\rho_{\text{in}}(x) = \frac{1}{2^N} \bigotimes_{i=1}^N \left[I + xX_i + \sqrt{1-x^2}Z_i \right], \quad (13)$$

where X_i and Z_i are X and Z rotations on the i th qubit, respectively. The density matrix can be generated by single-qubit rotations, $R_y(\sin^{-1} x)$ and $R_z(\cos^{-1} x^2)$ on each of the qubits. Our initial state is thus

$$|\psi_{\text{in}}(x)\rangle = \prod_{i=1}^N R_y^{(i)}(\sin^{-1} x) R_z^{(i)}(\cos^{-1} x^2) |0\rangle^{\otimes N}. \quad (14)$$

Note that in a practical numerical implementation, the continuous variable x must be made discrete. This initialization has the effect that the tensor-product state will be a polynomial of order N in x . However, the x^N term is hidden with the observable $X^{\otimes N}$. So in order to access its factor, we must use an entangling gate, which in this case has to be the diamond gate, $U(t)$. In order to create a parameterized quantum circuit, we apply a general single-qubit rotation $U_{\text{rot}}(\theta) = R_z(\theta_1)R_y(\theta_2)R_z(\theta_3)$ to each of the qubits. The pair of gates, $U(t)$ and $U_{\text{rot}}(\theta)$, are applied several times in layers, each with a different set of parameters. We use four such layers in our parameterized quantum circuit. At the end, we perform a measurement of the expectation value of Z on the first qubit, which we scale and shift to produce the output function, $F(x, \theta_i) = a\langle Z(x, \theta_i) \rangle + b$, where θ_i is the i th

tunable parameter of the circuit, from both $U(t)$ and $U_{\text{rot}}(\theta)$. The resulting gate diagram can be seen in Fig. 8.

We use the quadratic cost function, $L = \|f(x) - F(x, \theta_i)\|^2$ and optimize it using the ADAM optimizer [66]. We test our quantum circuit using the same objective functions as in Ref. [43], namely x^2 , e^x , $\sin x$, and $|x|$, as well as two more functions, $\sin(\pi x) \cos(\pi x/2)$ and $\sin(2\pi x)e^x$. We sample each objective function 100 times as training data. The results of the optimizations can be seen in Fig. 9. The parameterized quantum circuit approximates the function reasonably well, even though we only use four qubits and four layers, whereas in Ref. [43], six qubits and six layers are used to obtain the same precision. In Ref. [43], a fully connected transverse Ising model is used as the entangling gate, which is essentially equivalent to connecting all qubits with i SWAP gates, whereas we use the diamond gate to obtain the same results, showing that not only do we use fewer qubits and layers to achieve the same results but we also use fewer entangling operations per layer.

The reason why we obtain the same results as Ref. [43] with a more straightforward setup could be because the diamond gate is better at accessing the entire Hilbert space of the qubits compared to the transverse Ising model used in Ref. [43]. However, it should be mentioned that we optimize the operation time, t_j , of the diamond gate for each of the layers, whereas in Ref. [43] a constant time of operation is chosen for their entangling operation. This gives an extra optimization parameter per layer. This may not seem as much, especially when Ref. [43] has more rotation gates, but optimization of the parameters of the entangling operation could be a considerable advantage in quantum circuits.

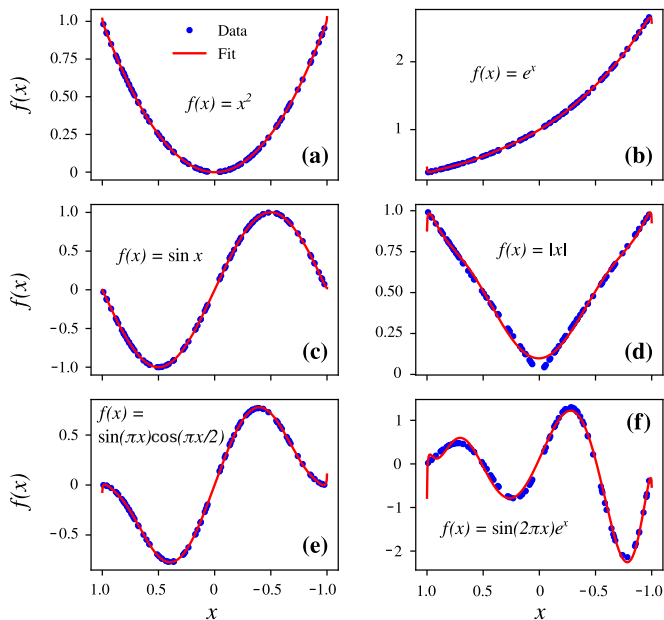


Figure 9. The data (blue points) and fit (red lines) obtained from the diamond-assisted quantum circuit learning using the quantum circuit seen in Fig. 8. The fit is given by the function $F(x, \theta_i)$ described in the main text. The parameters, θ_i , are tuned to minimize the cost function for all x . The function, $f(x)$, used to sample the blue data points shown, is as follows: (a) x^2 , (b) e^x , (c) $\sin x$, (d) $|x|$, (e) $\sin(\pi x) \cos(\pi x/2)$, and (f) $\sin(2\pi x)e^x$.

B. Classification of data

Another scheme for quantum machine learning that employs PQC is data-point classification. We employ a PQC with the diamond gate as the entangling gate and use it to classify two-dimensional data points. We follow the approach in Ref. [26] and use the same two-dimensional shapes in order to compare results directly.

The classification of data follows the same algorithm as quantum circuit learning (see Section VII A). However, here we use a different encoding, following the approach of Ref. [26]. This so-called *minimal expressive embedding* consists of applying single-qubit rotations like the encoding used previously. Thus instead of the encoding in Eq. (14), we use the following:

$$|\psi_{\text{in}}(x)\rangle = \prod_{i=1}^N R_z^{(i)}(\pi/4) R_y^{(i)}(\pi/4) R_x^{(i)}(x_i \bmod 2) |0\rangle^{\otimes N}, \quad (15)$$

where we first apply a rotation about the x axis, which depends on x_0 and x_1 in an alternating fashion. We then perform rotations of $\pi/4$ first around the y axis and then the z axis for all qubits. Following this input encoding, we apply the PQC consisting of the diamond gate, $U(t)$, and a set of general single-qubit rotations $U_{\text{rot}}(\theta)$ on each qubit. We apply these last two operations to the state several times, one for each layer that we want in our

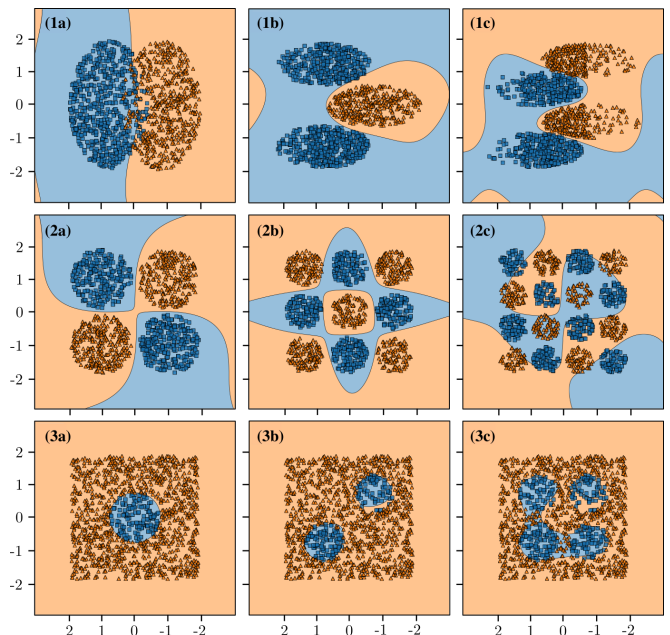


Figure 10. The diamond-assisted quantum circuit classification results of two-dimensional data points with two layers. The squares and triangles (blue and yellow) are the training data replicated from Ref. [26]. The background colors indicate the predicted classification by the quantum circuit.

model. In the end, we measure the expectation value of Z on the first qubit. The result is scaled, shifted, and then minimized using a binary cross-entropy function. Altogether, we perform the same manipulations as in Fig. 8 but with a different encoding, ρ_{in} .

In Fig. 10, we present the nine data sets as well as the classification results for two layers of $U(t)$ and $U_{\text{rot}}(\theta)$. We find the data sets (1b), (2a), and (3a) to be perfectly classified for just a single layer, as well as for more layers. Data set (1a) achieves a classification accuracy just above 95% for a single layer, which is the maximal for this data set due to the overlap of the data points. Data sets (2c) and (3b) also achieve a maximum classification accuracy for a single layer, of around 73% and 98%, respectively. Data sets (1c) and (2b) converge at a perfect accuracy for two layers, while the accuracy of the last data set (3c) converges for two layers to just above 90%.

We see almost perfect classification except for (2c) and (3c); however, these are most difficult due to their complexity. This performance is comparable to the most accurate two-layer networks used by Ref. [26]. Surprisingly, the classification performance of (2c) and (3c) does not improve when the number of layers increases from two to three. This might be because the expressibility of the PQCs is already saturated at two layers, meaning that a further increase of the depth of the circuits does not increase the available Hilbert space of the circuit [39, 57].

VIII. CONCLUSION AND OUTLOOK

We show that the native diamond gate [4] may be used beneficially compared to using standard gate sets, which makes it an auspicious architecture to realize on contemporary quantum technology platforms.

First, we show that the diamond gate, together with single-qubit gates, can be turned into a controlled-NOT SWAP gate. We then show how to symmetrically decompose the diamond gate into standard gates in two different ways. Also, by placing a diamond gate on either side of a phase gate, we create a controlled phase gate and argue that this could be used to obtain controlled-phase gates on all four qubits. Using this method, we present an algorithm for the quantum Fourier transform using only single-qubit gates and the diamond gate.

Finally, we apply the diamond gate in quantum

machine-learning algorithms and show that it was helpful in a parameterized quantum circuit when used to approximate nonlinear functions and classify two-dimensional data.

We believe that these results outline the diamond gate as a possible building block in near-future quantum technologies. This, together with the fact that other quantum gates do not occur naturally in many quantum technology schemes, demonstrates that the applications of the diamond gate should be pursued further.

ACKNOWLEDGMENTS

We would like to thank L. B. Kristensen for discussions on different aspects of the work. This work is supported by the Danish Council for Independent Research and the Carlsberg Foundation, and is derived from E.B.'s Master's thesis [67].

-
- [1] F. Arute, K. Arya, R. Babbush, D. Bacon, J. C. Bardin, R. Barends, R. Biswas, S. Boixo, F. G. S. L. Brandao, D. A. Buell, B. Burkett, Y. Chen, Z. Chen, B. Chiaro, R. Collins, W. Courtney, A. Dunsworth, E. Farhi, B. Foxen, A. Fowler, C. Gidney, M. Giustina, R. Graff, K. Guerin, S. Habegger, M. P. Harrigan, M. J. Hartmann, A. Ho, M. Hoffmann, T. Huang, T. S. Humble, S. V. Isakov, E. Jeffrey, Z. Jiang, D. Kafri, K. Kechedzhi, J. Kelly, P. V. Klimov, S. Knys, A. Korotkov, F. Kostritsa, D. Landhuis, M. Lindmark, E. Lucero, D. Lyakh, S. Mandrà, J. R. McClean, M. McEwen, A. Megrant, X. Mi, K. Michielsen, M. Mohseni, J. Mutus, O. Naaman, M. Neeley, C. Neill, M. Y. Niu, E. Ostby, A. Petukhov, J. C. Platt, C. Quintana, E. G. Rieffel, P. Roushan, N. C. Rubin, D. Sank, K. J. Satzinger, V. Smelyanskiy, K. J. Sung, M. D. Trevithick, A. Vainsencher, B. Villalonga, T. White, Z. J. Yao, P. Yeh, A. Zalcman, H. Neven, and J. M. Martinis, *Nature* **574**, 505 (2019).
- [2] S. Bravyi, D. Gosset, R. König, and M. Tomamichel, *Nature Physics* (2020), 10.1038/s41567-020-0948-z.
- [3] J. Preskill, *Quantum* **2**, 79 (2018).
- [4] N. J. S. Loft, M. Kjaergaard, L. B. Kristensen, C. K. Andersen, T. W. Larsen, S. Gustavsson, W. D. Oliver, and N. T. Zinner, *npj Quantum Information* **6**, 47 (2020).
- [5] M. A. Nielsen and I. L. Chuang, *Quantum Computation and Quantum Information* (Cambridge University Press, Cambridge, UK, 2010).
- [6] G. J. Milburn, *Phys. Rev. Lett.* **62**, 2124 (1989).
- [7] H. F. Chau and F. Wilczek, *Phys. Rev. Lett.* **75**, 748 (1995).
- [8] J. Fiurášek, *Phys. Rev. A* **73**, 062313 (2006).
- [9] J. Fiurášek, *Phys. Rev. A* **78**, 032317 (2008).
- [10] Y.-X. Gong, G.-C. Guo, and T. C. Ralph, *Phys. Rev. A* **78**, 012305 (2008).
- [11] R. B. Patel, J. Ho, F. Ferreyrol, T. C. Ralph, and G. J. Pryde, *Science Advances* **2** (2016), 10.1126/sciadv.1501531.
- [12] T. Ono, R. Okamoto, M. Tanida, H. F. Hofmann, and S. Takeuchi, *Scientific Reports* **7**, 45353 EP (2017), article.
- [13] J. A. Smolin and D. P. DiVincenzo, *Phys. Rev. A* **53**, 2855 (1996).
- [14] T. Bækkegaard, L. B. Kristensen, N. J. S. Loft, C. K. Andersen, D. Petrosyan, and N. T. Zinner, *Scientific Reports* **9**, 13389 (2019).
- [15] S. Poletto, J. M. Gambetta, S. T. Merkel, J. A. Smolin, J. M. Chow, A. D. Córcoles, G. A. Keefe, M. B. Rothwell, J. R. Rozen, D. W. Abraham, C. Rigetti, and M. Steffen, *Phys. Rev. Lett.* **109**, 240505 (2012).
- [16] S. E. Rasmussen, K. S. Christensen, and N. T. Zinner, *Phys. Rev. B* **99**, 134508 (2019).
- [17] S. E. Rasmussen, K. Groenland, R. Gerritsma, K. Schoutens, and N. T. Zinner, *Phys. Rev. A* **101**, 022308 (2020).
- [18] E. Farhi, J. Goldstone, and S. Gutmann, “A quantum approximate optimization algorithm,” (2014), arXiv:1411.4028.
- [19] J. S. Otterbach, R. Manenti, N. Alidoust, A. Bestwick, M. Block, B. Bloom, S. Caldwell, N. Didier, E. S. Fried, S. Hong, P. Karalekas, C. B. Osborn, A. Papageorge, E. C. Peterson, G. Prawiroatmodjo, N. Rubin, C. A. Ryan, D. Scarabelli, M. Scheer, E. A. Sete, P. Sivarajah, R. S. Smith, A. Staley, N. Tezak, W. J. Zeng, A. Hudson, B. R. Johnson, M. Reagor, M. P. da Silva, and C. Rigetti, “Unsupervised machine learning on a hybrid quantum computer,” (2017), arXiv:1712.05771.
- [20] N. Moll, P. Barkoutsos, L. S. Bishop, J. M. Chow, A. Cross, D. J. Egger, S. Filipp, A. Fuhrer, J. M. Gambetta, M. Ganzhorn, A. Kandala, A. Mezzacapo, P. Muller, W. Riess, G. Salis, J. Smolin, I. Tavernelli, and K. Temme, *Quantum Science and Technology* **3**, 030503 (2018).
- [21] J. Romero, J. P. Olson, and A. Aspuru-Guzik, *Quantum Sci. Technol.* **2**, 045001 (2017).
- [22] P. D. Johnson, J. Romero, J. Olson, Y. Cao, and A. Aspuru-Guzik, “Qvector: an algorithm for device-tailored quantum error correction,” (2017),

- arXiv:1711.02249.
- [23] E. Farhi and H. Neven, “Classification with quantum neural networks on near term processors,” (2018), arXiv:1802.06002.
- [24] V. Havlíček, A. D. Córcoles, K. Temme, A. W. Harrow, A. Kandala, J. M. Chow, and J. M. Gambetta, *Nature* **567**, 209 (2019).
- [25] M. Schuld, A. Bocharov, K. M. Svore, and N. Wiebe, *Phys. Rev. A* **101**, 032308 (2020).
- [26] T. Hubregtsen, J. Pichlmeier, P. Stecher, and K. Bertels, “Evaluation of parameterized quantum circuits: on the design, and the relation between classification accuracy, expressibility and entangling capability,” (2020), arXiv:2003.09887.
- [27] P.-L. Dallaire-Demers and N. Killoran, *Phys. Rev. A* **98**, 012324 (2018).
- [28] S. Lloyd and C. Weedbrook, *Phys. Rev. Lett.* **121**, 040502 (2018).
- [29] C. Zoufal, A. Lucchi, and S. Woerner, *npj Quantum Information* **5**, 103 (2019).
- [30] D. Zhu, N. M. Linke, M. Benedetti, K. A. Landsman, N. H. Nguyen, C. H. Alderete, A. Perdomo-Ortiz, N. Korda, A. Garfoot, C. Brecque, L. Egan, O. Perdomo, and C. Monroe, *Science Advances* **5**, eaaw9918 (2019).
- [31] A. Peruzzo, J. McClean, P. Shadbolt, M.-H. Yung, X.-Q. Zhou, P. J. Love, A. Aspuru-Guzik, and J. L. O’Brien, *Nature Communications* **5**, 4213 (2014).
- [32] J. R. McClean, J. Romero, R. Babbush, and A. Aspuru-Guzik, *New Journal of Physics* **18**, 023023 (2016).
- [33] P. J. J. O’Malley, R. Babbush, I. D. Kivlichan, J. Romero, J. R. McClean, R. Barends, J. Kelly, P. Roushan, A. Tranter, N. Ding, B. Campbell, Y. Chen, Z. Chen, B. Chiaro, A. Dunsworth, A. G. Fowler, E. Jeffrey, E. Lucero, A. Megrant, J. Y. Mutus, M. Neeley, C. Neill, C. Quintana, D. Sank, A. Vainsencher, J. Wenner, T. C. White, P. V. Coveney, P. J. Love, H. Neven, A. Aspuru-Guzik, and J. M. Martinis, *Phys. Rev. X* **6**, 031007 (2016).
- [34] A. Kandala, A. Mezzacapo, K. Temme, M. Takita, M. Brink, J. M. Chow, and J. M. Gambetta, *Nature* **549**, 242 (2017).
- [35] Y. Cao, J. Romero, J. P. Olson, M. Degroote, P. D. Johnson, M. Kieferová, I. D. Kivlichan, T. Menke, B. Peropadre, N. P. D. Sawaya, S. Sim, L. Veis, and A. Aspuru-Guzik, *Chemical Reviews* **119**, 10856 (2019).
- [36] P. K. Barkoutsos, J. F. Gonthier, I. Sokolov, N. Moll, G. Salis, A. Fuhrer, M. Ganzhorn, D. J. Egger, M. Troyer, A. Mezzacapo, S. Filipp, and I. Tavernelli, *Phys. Rev. A* **98**, 022322 (2018).
- [37] A. J. McCaskey, Z. P. Parks, J. Jakowski, S. V. Moore, T. D. Morris, T. S. Humble, and R. C. Pooser, *npj Quantum Information* **5**, 99 (2019).
- [38] B. T. Gard, L. Zhu, G. S. Barron, N. J. Mayhall, S. E. Economou, and E. Barnes, *npj Quantum Information* **6**, 10 (2020).
- [39] S. Sim, P. D. Johnson, and A. Aspuru-Guzik, *Advanced Quantum Technologies* **2**, 1900070 (2019).
- [40] M. R. Geller, *Phys. Rev. Applied* **10**, 024052 (2018).
- [41] Y. Du, M.-H. Hsieh, T. Liu, and D. Tao, *Phys. Rev. Research* **2**, 033125 (2020).
- [42] M. Benedetti, E. Lloyd, S. Sack, and M. Fiorentini, *Quantum Science and Technology* **4**, 043001 (2019).
- [43] K. Mitarai, M. Negoro, M. Kitagawa, and K. Fujii, *Phys. Rev. A* **98**, 032309 (2018).
- [44] S. E. Rasmussen, N. J. S. Loft, T. Bækkegaard, M. Kues, and N. T. Zinner, *Advanced Quantum Technologies* **3**, 2000063 (2020).
- [45] J. Koch, T. M. Yu, J. Gambetta, A. A. Houck, D. I. Schuster, J. Majer, A. Blais, M. H. Devoret, S. M. Girvin, and R. J. Schoelkopf, *Phys. Rev. A* **76**, 042319 (2007).
- [46] J. A. Schreier, A. A. Houck, J. Koch, D. I. Schuster, B. R. Johnson, J. M. Chow, J. M. Gambetta, J. Majer, L. Frunzio, M. H. Devoret, S. M. Girvin, and R. J. Schoelkopf, *Phys. Rev. B* **77**, 180502 (2008).
- [47] N. Schuch and J. Siewert, *Phys. Rev. A* **67**, 032301 (2003).
- [48] T. Tanamoto, K. Maruyama, Y.-x. Liu, X. Hu, and F. Nori, *Phys. Rev. A* **78**, 062313 (2008).
- [49] T. Tanamoto, Y.-x. Liu, X. Hu, and F. Nori, *Phys. Rev. Lett.* **102**, 100501 (2009).
- [50] J. Q. You and F. Nori, *Physics Today* **58**, 42 (2005), <https://doi.org/10.1063/1.2155757>.
- [51] A. M. Zagoskin, S. Ashhab, J. R. Johansson, and F. Nori, *Phys. Rev. Lett.* **97**, 077001 (2006).
- [52] D. C. McKay, S. Filipp, A. Mezzacapo, E. Magesan, J. M. Chow, and J. M. Gambetta, *Phys. Rev. Applied* **6**, 064007 (2016).
- [53] A. Dewes, F. R. Ong, V. Schmitt, R. Lauro, N. Boulant, P. Bertet, D. Vion, and D. Esteve, *Phys. Rev. Lett.* **108**, 057002 (2012).
- [54] Y. Salathé, M. Mondal, M. Oppliger, J. Heinsoo, P. Kurpiers, A. Potočnik, A. Mezzacapo, U. Las Heras, L. Lamata, E. Solano, S. Filipp, and A. Wallraff, *Phys. Rev. X* **5**, 021027 (2015).
- [55] U. Vool and M. Devoret, *International Journal of Circuit Theory and Applications* **45**, 897 (2017).
- [56] P. Krantz, M. Kjaergaard, F. Yan, T. P. Orlando, S. Gustavsson, and W. D. Oliver, *Applied Physics Reviews* **6**, 021318 (2019).
- [57] S. Rasmussen, K. Christensen, S. Pedersen, L. Kristensen, T. Bækkegaard, N. Loft, and N. Zinner, *PRX Quantum* **2**, 040204 (2021).
- [58] A. Imamoglu, D. D. Awschalom, G. Burkard, D. P. DiVincenzo, D. Loss, M. Sherwin, and A. Small, *Phys. Rev. Lett.* **83**, 4204 (1999).
- [59] M. Benito, J. R. Petta, and G. Burkard, *Phys. Rev. B* **100**, 081412R (2019).
- [60] A. Blais, R.-S. Huang, A. Wallraff, S. M. Girvin, and R. J. Schoelkopf, *Phys. Rev. A* **69**, 062320 (2004).
- [61] H.-F. Wang, X.-Q. Shao, Y.-F. Zhao, S. Zhang, and K.-H. Yeon, *J. Opt. Soc. Am. B* **27**, 27 (2010).
- [62] M. Bartkowiak and A. Miranowicz, *J. Opt. Soc. Am. B* **27**, 2369 (2010).
- [63] C. Godfrin, R. Ballou, E. Bonet, M. Ruben, S. Klyatskaya, W. Wernsdorfer, and F. Balestro, *npj Quantum Information* **4**, 53 (2018).
- [64] S. E. Rasmussen and N. T. Zinner, *Phys. Rev. Research* **2**, 033097 (2020).
- [65] T. Kim and B.-S. Choi, *Scientific Reports* **8**, 5445 (2018).
- [66] D. P. Kingma and J. Ba, “Adam: A method for stochastic optimization,” (2014), arxiv:1412.6980.
- [67] E. Bahnsen, “Native gate exploitation in four-qubit quantum circuit creation,” (2020), <https://www.bahnsen.dev/masters>.

Appendix A: Alternative topologies for the QFT algorithm with the diamond gate

There are several other ways to combine the diamond gate for the QFT algorithm. Here we discuss two other approaches which might lessen unwanted cross talk and frequency crowding.

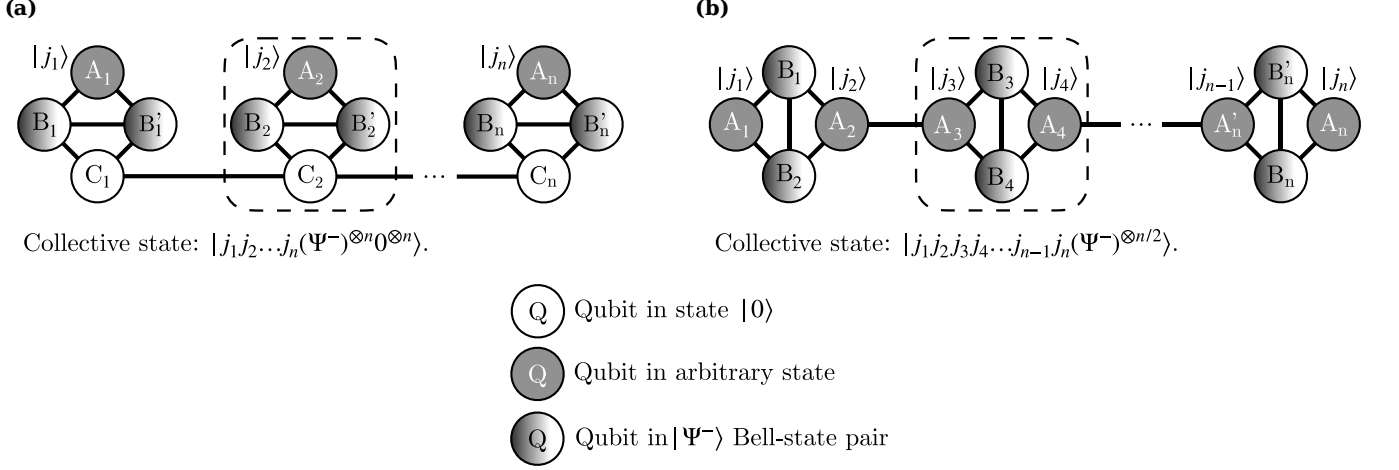


Figure 11. Alternative (to Fig. 7) arrangements of multiple diamond circuits interconnected to form a string to execution the diamond gate-assisted QFT algorithm. **(a)** The algorithm used for this can be seen in Algorithm 2. With this topology, we make use of the idle-state of the diamond, the CNS-gate, and the diamond-assisted method of performing a CR_n -gate of Fig. 4. **(b)** This configuration is very similar to that of **(a)**, except that we must be more careful when we use the CNS-gate to swap states. This uses two qubits for every input state, as opposed to four.

An example of such an alternative arrangement of the qubits is seen in Fig. 11(a). Here each diamond is connected via one of the target qubits. The control gates must be prepared in a $|\Psi^-\rangle$ state in order to exploit the idle state of the diamond gate. The non-connected target qubits, A_i , are prepared as the input states, while the connected qubits, C_i s, are prepared in the $|0\rangle$ state. Besides using the idle state of the diamond gate, we also employ the CNS gate. With all C-qubit states being $|0\rangle$, we can swap the states of each A- and C-qubit pair before this state moves on. Each time the state passes a diamond gate, we perform a CR_n gate as described in Section V. The algorithm used can be seen in Algorithm 2.

Algorithm 2 Native gate assisted QFT on string of diamonds [Fig. 11(b)]

- 1: Initialize qubits A_1, \dots, A_n with the states to transform $(|j_1\rangle, \dots, |j_n\rangle)$
 - 2: Initialize qubits C_1, \dots, C_n in state $|0\rangle$
 - 3: Initialize qubit pairs $(B_1, B'_1), \dots, (B_n, B'_n)$ in state $|\Psi^-\rangle$
 - 4: **for** $i = 1$ **to** n **do**
 - 5: H on A_i
 - 6: Set qubits B_i and B'_i to $|0\rangle$
 - 7: Swap state of A_i and C_i with diamond CNS-gate
 - 8: Set qubit pair (B_i, B'_i) to $|\Psi^-\rangle$
 - 9: **for** $j = i + 1$ **to** n **do**
 - 10: *i*SWAP $(t_g/2)$ on (C_{j-1}, C_j)
 - 11: Set qubits B_j and B'_j to $|0\rangle$
 - 12: *i*SWAP $(t_g/2)$ on (A_j, B_j)
 - 13: R_{j-i+1} on C_j controlled by B_j (using Fig. 4)
 - 14: *i*SWAP $(3t_g/2)$ on (A_j, B_j)
 - 15: Set qubit pair (B_j, B'_j) to $|\Psi^-\rangle$
 - 16: **end for**
 - 17: Swap state of C_n back to C_i with *i*SWAP $(3t_g/2)$ or correct for number of *i*SWAP $(t_g/2)$'s along C-chain (mod 4) and readout state.
 - 18: **end for**
 - 19: Reverse order of C-qubits (these are the output qubits).
-

Another approach to the arrangement of the diamond gates can be seen in Fig. 11(b). In this case, only two qubits are used per input state, as opposed to the example in Fig. 11(a) where four qubits were used. Like the example in

Fig. 11(a), it employs the idle state of the diamond, the CR_n gate, and the CNS gate. Using this approach, we preserve the input state that is being transformed. The target of the CNS gate acts on the other qubit and not the one currently being transformed. This is similar to the CNS based pseudo-swap used in Section VI B.

The algorithm associated with Fig. 11(b) is similar to the one in Algorithm 2. They both use three out of four control states of the diamond gate, $|00\rangle$, $|11\rangle$, and $|\Psi^-\rangle$. Both have the same circuit depth, $O(n^2)$, which can be reduced to $O(n \log n)$ with an approximate QFT approach.

Appendix B: QFT algorithm for four qubits

Here we present an example of the QFT algorithm for the four qubits in Fig. 12. The final cross-swap is not shown, such that it is clear when each qubit has reached their final state. Dotted lines shows the diamond circuit in use.

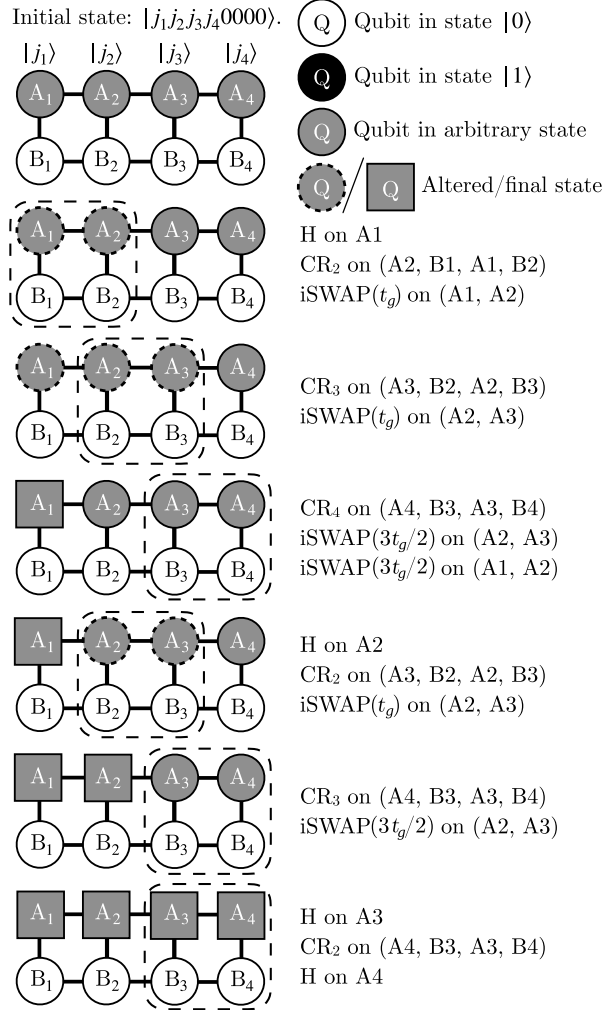


Figure 12. Example of the native gate-assisted QFT algorithm for input size $n = 4$. The final cross-swap of A-qubits is not shown, such that the timing of the final states is highlighted. The dotted lines show the diamond part of the circuit in use for each step